16

The Interdependence of Exposure and Development Conditions when Optimizing Low-Energy EBL for Nano-Scale Resolution

Mohammad A. Mohammad[1], Taras Fito[1,2], Jiang Chen[2], Steven Buswell[3], Mirwais Aktary[3], Steven K. Dew[1] and Maria Stepanova[2]
[1]*Department of Electrical and Computer Engineering, University of Alberta,*
[2]*National Institute for Nanotechnology NRC,*
[3]*Applied Nanotools Inc.*
Canada

1. Introduction

Electron beam lithography (EBL) is the major direct-write technique to controllably fabricate nanoscale features. A focused beam of electrons induces a chemical change in a layer of radiation sensitive material (resist), such as chain scissioning in positive tone polymethylmethacrylate (PMMA) polymer photoresist. The localized fragmented region is rendered more soluble in a suitable developer solution and removed. In negative tone resists, such as hydrogen silsesquioxane (HSQ) or calixarene, the radiation damage eventually results in bond cross-linking, generating structures locally more resistant to dissolution. Limitations of the technology are related largely with unwanted exposure of the resist away from the impact of the focused electron beam due to scattering of the primary electrons in the resist (often described as the forward scattering), generation of secondary electrons, and backscattering from the substrate (the proximity effect). The exposure and development processes have been optimized and routinely used for fabrication of submicron features. However, as requirements for lithography have progressed toward the sub-20 nm regimes, major challenges have emerged of introducing controllable radiation-induced changes at molecular-size scales, within a reasonable tradeoff with the applicability of the standard materials, as well as cost and simplicity of the processes. Due to the proximity effect, this becomes particularly demanding when dense patterns with closely positioned features must be fabricated. Achieving deep nanoscale resolutions in high density patterns at industrially-relevant throughputs requires new approaches to EBL.

Novel EBL processes that would extend capabilities of the technology significantly into the deep nanoscale regime entail new approaches to resist design, exposure strategies, and development techniques (Häffner et al., 2007; Liddle et al., 2003; Ocola & Stein, 2007; Word et al., 2003). To achieve this will require a much more detailed understanding of the molecular mechanisms involved in both the electron-resist interaction and in the polymer dissolution (development) stages of the nanolithography process. Despite a significant research effort and vast literature on electron beam lithography, the detailed molecular mechanisms are still inadequately understood. Published modeling studies address

Source: Lithography, Book edited by: Michael Wang,
ISBN 978-953-307-064-3, pp. 656, February 2010, INTECH, Croatia, downloaded from SCIYO.COM

extensively the processes of electron penetration, scattering, and energy deposition in resist and substrate materials (Kyser & Viswanathan, 1975; Murata et al., 1981; Lee et al., 1992; Raptis et al, 1993; Raptis et al, 2001; Zhou & Yang, 2006), however, the analyses of exposure of resists are mostly limited to conversions of the average amounts of energy deposited by electrons into the average number of relevant molecular events, such as the bond scissions, through the empirically determined radiation chemical yield (Chapiro, 1962; Greeneich, 1974; Han et al., 2003; Kyser & Viswanathan, 1975; Raptis et al., 2001). Furthermore, the detailed molecular processes occurring during dissolution of the most useful resists have been under-addressed if not overlooked so far. As a consequence, understanding of the trends of resist development currently resides mostly on published experimental results (Cord et al., 2007; Dial et al., 1998; Ocola & Stein, 2006; Yan et al., 2008; Yasin et al., 2002; Yasin et al., 2004).

Within the last decade, numerous research groups have invested a significant effort to explore experimentally the resolution limits of deep nanoscale EBL. In particular, optimizing the development conditions such as the developer formula (Dial et al., 1998; Yan et al., 2008; Yasin et al. 2002) and development temperature (Cord et al., 2007; Ocola & Stein, 2006; Yan et al., 2008) have been found effective to achieve improvements in resolution below the 20 nm mark. However, these works were conducted by employing exposures with relatively high beam energies of at least 30 keV or higher. Increasing the acceleration voltages allows for easier fabrication of high-resolution structures due to reduced forward scattering and reduced aspect ratio requirements; however, this approach has its disadvantages. High voltage processes are generally more expensive and have a lower throughput due to the increased exposure dose requirement. High energy electrons also tend to penetrate deep in the substrate causing unwanted substrate damage, as well as give rise to a significant proximity effect. In contrast, ultra low voltage electrons in the 1-3 keV regimes deposit most of their energy within the resist, resulting in less substrate damage and decreasing dramatically the proximity effect (Lee et al., 1992; Schock et al., 1997). Furthermore, exposures employing voltages below 10 keV require lower doses roughly in proportion to the acceleration voltage (Schock et al., 1997). Strong forward scattering of low energy electrons, which is routinely believed to be the major resolution-limiting factor, may alternatively be employed to create nanoscale three-dimensional profiles in the resist (Brünger et al., 1995). Realizing this potential, however, requires a thorough, systematic understanding of the intricate interplay of the numerous process control parameters including the accelerating voltage, optimum exposure dose, and the favorable conditions of development. Clearly, this systematic understanding should rely on a solid knowledge of the physico-chemical molecular-level processes behind the resist exposure to electrons as well as the subsequent post-exposure development stages.

Over the last several years we have been investigating thoroughly, both experimentally and by numeric modeling, the impact of the major EBL process factors on the quality of dense nanoscale patterns in the popular positive-tone resist, PMMA (Aktary et al., 2006; Mohammad et al., 2007; Mohammad et al., 2009, Fito et al., 2009). In this chapter, we outline the methodologies that we have developed for fabrication and visualization of nanopatterns in PMMA, as well as our model for the exposure, fragmentation, and dissolution of positive resists. We discuss the results of our systematic study of the impact of the exposure dose, duration of development, temperature of developer, and other process conditions on the quality and process sensitivity of dense nanoscale gratings fabricated using low to medium (3-30keV) exposure energies. The focus of the discussion comprises dense patterns of 15-35

nm features in 45-70 nm thick PMMA resist. We demonstrate that, in addition to the exposure conditions that are routinely optimized in standard EBL techniques, post-exposure resist processing is also a crucial factor and should be co-optimized when fabricating the dense nanopatterns. We analyze the tradeoff of the dose requirements and pattern quality when employing low-voltage exposures combined with cold development, and discuss possible optimized solutions to ultimately push the limit of EBL toward the nanometer-scale resolution. We also discuss the research challenges related with the molecular mechanisms of development, which should be understood thoroughly in order to efficiently optimize the EBL process.

2. Fabrication, visualization, and quality control of nanostructures in PMMA

In our work, we have studied systematically the morphologies that we fabricated in the most popular positive resist, PMMA, using low to medium energy EBL. We consider dense arrays of periodic lines (gratings) as a convenient benchmark nanostructure. Employing these grating patterns, we analyze typical morphology regimes, which we visualize by SEM, as a function of the various process conditions. We interpret the conventional characteristics of the EBL process, such as the resolution and sensitivity, in terms of the quality of the fabricated nanoscale morphologies. We believe that the morphology-bound interpretations of the sensitivity and resolution adopted in our work are more relevant to characterize EBL nanofablication than the often-employed studies of the resist contrast curves, since the first approach is directly representative of the quality of fabricated nanostructures.

2.1 Nanoscale morphologies of dense gratings in PMMA

The experimental methodology that we have employed has been described in detail elsewhere (Mohammad et al., 2007). In brief, cleaned silicon substrates were spin coated with 950k mol. wt. PMMA providing a nominally 65 nm thick layer. As the next stage, sets of periodic grating patterns were generated by electron beam lithography (Raith 150). The incident electron energy used was typically 10 keV with a beam diameter of 2 nm. The layout of our grating design represented an array of grating units, each of which consisted of a set of parallel, 2 nm wide exposed lines of a given pitch. We have generated multiple sets of parallel lines with the spacing varying from 20 nm to 100 nm, and various exposure doses. Each set of parallel lines covered a lateral distance of 2 μm in width, in order to ensure a uniform cumulative exposure due to backscattered electrons in the central portion of the set. The exposed patterns were developed using a standard procedure of dipping the substrates in a 1:3 MIBK: IPA developer followed by an IPA stopper rinse and drying the substrates with a nitrogen gun. As a final step before imaging our samples (Hitachi S-4800 FE-SEM), we coated our substrates by sputtering (Kurt J. Lesker Co.) an approximately 6 nm thick Chromium as an anti-charging layer.

In the discussion below, we employ two descriptors for the exposure dose: the *average area dose* and the *line dose*. For gratings, these dose descriptors are related by $d_{(area)} = d_{(line)}/\lambda$, where λ is the interline distance (grating pitch). Employing the area dose is more convenient for comparisons of dense nanopatterns of various shapes, whereas the line dose is more straightforward for use when analyzing process conditions for gratings of a given width. Below we employ the different approaches according to the subject discussed.

Fig. 1 shows a representative selection of morphologies that we have obtained experimentally after 5 sec development of high-density gratings with various interline

spacings generated with various exposure doses using 10 keV electrons. From the figure, it is evident that the potential to fabricate a quality grating is strongly dependent on both the exposure dose and the interline distance. Thus, for 70 nm pitch, all the images present well developed gratings, with the exception of Fig. 1(d) that corresponds to the high area dose of

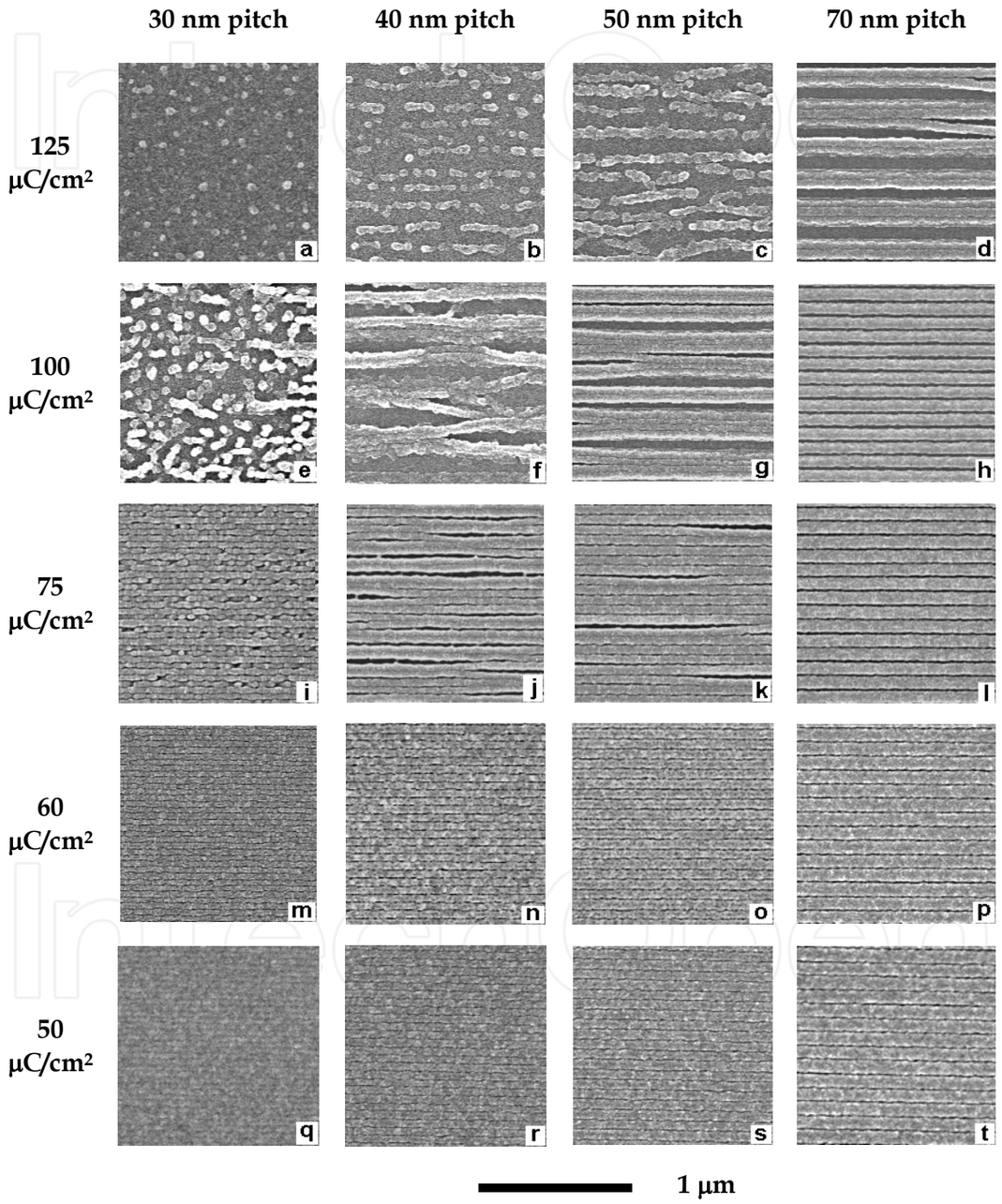

Fig. 1. SEM images of 30 nm, 40 nm, 50 nm, and 70 nm gratings fabricated in a 65-nm thick PMMA layer on a silicon substrate, with 10 keV electrons, at the various area doses. The gratings were developed for 5 sec. in a 1:3 MIBK:IPA solution at room temperature. The lateral size of all images is 1 μm×1 μm (Mohammad et al., 2007).

125 μC/cm². For 40 nm and 50 nm gratings, promising morphologies are seen in Figs. 1(n), 1(o), and 3(k) for the doses from 50 to 75 μC/cm². For 30 nm interline distance, only Fig. 3(m) for 60 μC/cm² exhibits a promising morphology. The other images in Fig.1 show various damaging influences. The first and well-known one is underexposure, when the clearance depth of exposed lines is insufficient to generate a grating pattern. In our SEM images, this is manifested by a low contrast as shown in Figs. 1(q), 1(m), and 1(r). The other extreme regime is overexposure, when the pattern is damaged by excessive clearance of PMMA. Strongly overexposed are the gratings in Figs. 1(a) and 1(b), which were obtained with the area dose of 125 μC/cm². Mild signs of overexposure are also visible in Figs. 1 (c) and (e) for 125 and 100 mC/cm², respectively. The next typical kind of morphology is the collapse of interline walls. Examples of collapsed gratings are given in Figs. 1(d), 1(f), and 1(g). Some collapse is also apparent in Figs. 1(j) and, to a lesser extent, in Fig. 1(k). It is noteworthy that collapse only occurs in gratings with 40 nm and larger pitch. In 30 nm gratings the limiting mechanism is different as illustrated in Fig. 1(e) and 1(i). In these cases, the grating is partly or entirely destroyed by redistribution of PMMA that tends to form islands at irregular locations. Similar morphologies have been reported in the literature for PMMA uniformly exposed to electrons and then developed (Hasko et al., 2000; Yasin et al., 2004). It is well known that formation of globular islands or percolation networks may occur in immiscible liquids that undergo a phase separation generating such morphologies as seen in Fig. 1(e). Since mixtures of PMMA fragments with most common EBL developers have regimes of limited miscibility, a phase separation can occur. The underlying mechanism would comprise relocation of individual molecules of PMMA driven by thermodynamic forces associated with the surface tension between the insoluble PMMA fraction and the developer. In our works we denote this mechanism as micellization, to emphasize the expected involvement of solventophobic interactions resulting in phase separation (Mohammad et al., 2007).

To summarize, we observe four factors that may damage the resist morphology. Two of those factors, underexposure and overexposure, are directly related to the electron dose applied, whereas the other two, micellization and collapse, are post-exposure processes of resist degradation. In the first case, degradation seems to occur through redistribution of individual PMMA molecules, whereas in the second case, entire interline walls are bent or displaced from their initial locations.

In addition to plan-view imaging of the grating morphologies in PMMA, we also visualized the cross-sectional profiles of such structures. Our methodology comprises exposure of long (up to 2 mm) grating patterns, which are then developed and blown dry using nitrogen gas. To generate crisp cross sections, the samples were manually cleaved when dipped in liquid nitrogen to achieve a clean fracture and prevent the resist deformation. Before SEM imaging, we coated our substrates with 4-6 nm of chromium.

A SEM image of a cleaved sample is shown in Fig. 2, and Fig. 3 demonstrates crisp cross sections representing a well-done grating pattern, an underexposed pattern, and a collapsed pattern With this information on three-dimensional structure of the typical surface morphologies, the mechanisms of the resist's development as well as degradation, such as collapse, can be understood significantly better than from plan-view images alone.

2.2 Applicable exposure dose windows, resolution, and sensitivity

Fig. 4 summarizes the observed morphologic regimes for various grating periods and exposure doses. In the low dose regime, the limiting factor is underexposure, whereas at

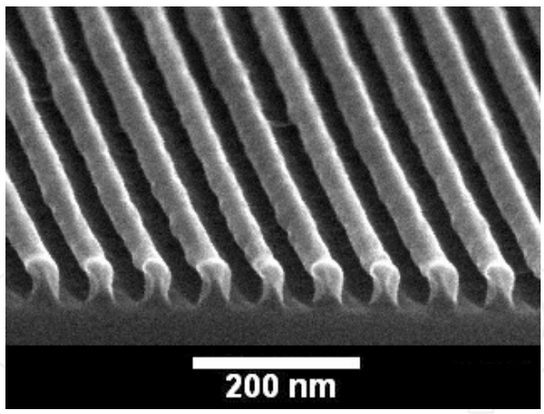

Fig. 2. SEM micrograph of a cleaved grating in PMMA on a Si substrate.

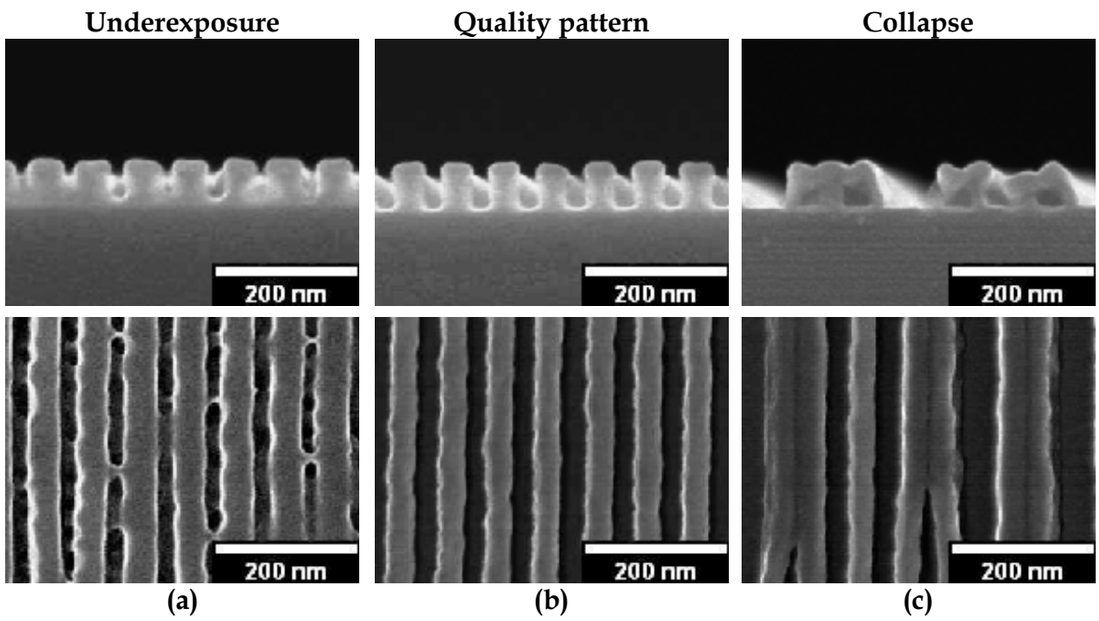

Fig. 3. Examples for (a) under-exposed, (b) well-done, and (c) collapsed gratings in PMMA, imaged by cross-sectional profiles (top) and plan-views (bottom).

increased doses, the patterns degrade through micellization or collapse. The densest gratings, with periods of 20 and 30 nm, degrade through micellization, and the gratings with periods of 40 nm and larger rather tend to collapse. At even higher doses, we observe overexposed patterns that are also micellized for all gratings pitches.

It can be seen that the window of favourable exposure doses at which quality gratings can be expected decreases rapidly when the grating pitch decreases. The explanation is that at the deep nanoscale, the electron beam broadening becomes comparable with the interline distance, and the unwanted exposure of the resist between the lines becomes stronger. Generally, the width of the applicable dose window represents the robustness of the process. A large dose window means that the fabrication process has improved reproducibility, and also has greater controllability over the line width and aspect ratio. The minimum size of nanostructures for which a reasonable dose window is attained

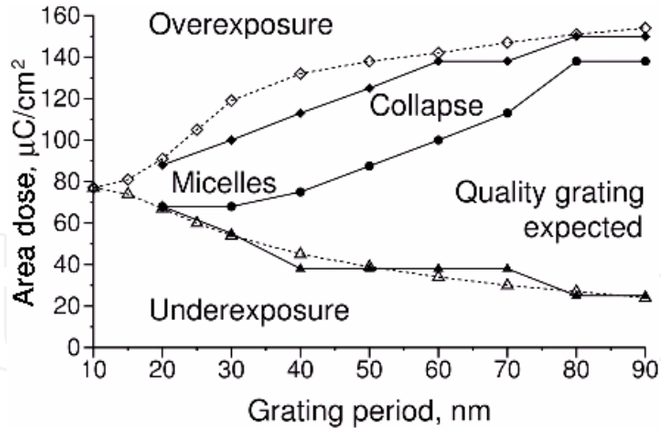

Fig. 4. Diagram of the characteristic morphologies in PMMA for various grating periods and area exposure doses using 10 keV voltage. Filled symbols show experimental results for the conditions as in Fig.1: triangles denote the boundary for underexposure (insufficient clearance); diamonds denote the boundary for overexposure (excessive clearance), and circles indicate the boundary for collapse or micellization. Open symbols show the results of numerical modeling of clearance as discussed in Sect. 3.2. (Mohammad et al., 2007).

characterizes the resolution. From Fig. 4 it follows that the highest resolution attainable at the experimental conditions considered corresponds to approximately 30 nm pitch (or approximately 15 nm half-pitch representing the average line width).

The minimum applicable doses can be associated with the sensitivity of the EBL process. In Fig. 4, the boundary dose for underexposure decreases when the grating pitch increases. The explanation is that in periodic gratings, the exposure dose per line at which the depth clearance is achieved can be viewed as independent of the interline distance. This leads to the corresponding dose per unit area decreasing roughly in proportion to the inverse of the period (Mohammad et al., 2007).

2.3 Cold development of PMMA broadens the applicable dose windows

Next, we have studied the influence of the development temperature on the nanoscale resolution and sensitivity of EBL using PMMA as the resist (Mohammad et al., 2009). We employed 47-55 nm thick layers of 950k PMMA on a Si substrate, a 10 keV exposure voltage, an 1:3 MIBK:IPA mixture for developer, and IPA for stopper. We varied the developer and stopper temperature between -15 °C and 22 °C using a cold plate, and experimented with development times from 5 sec to 20 sec. The stopper temperature was the same as that of the developer. Our approach was to determine the applicable dose windows for fabrication of quality grating patterns by varying the exposure doses and investigating the corresponding plan-view SEM images for various conditions of development.

Figs. 5 (a) and (b) present favorable windows for *line* exposure doses as functions of the development time, at various developer temperatures, for gratings with 70 nm and 50 nm pitches, respectively. In the figures, the solid lines show dose boundaries for underexposure (see Fig. 3(a)), and the dashed lines show the boundaries for collapse (Fig. 3(c)). The regions between the solid and dashed lines represent the favorable dose windows where quality gratings may be fabricated. It can be seen that in a grating with 70 nm pitch, decreasing the development temperature from room temperature (RT) to -15 °C results in an increase in the

applicable line dose window by an order of magnitude. In gratings with 50 nm pitch, the dose window increases approximately twice when the development temperature changes from -5 °C to -15 °C. This indicates a strong improvement in the EBL process resolution when decreasing the development temperature from RT to –5-15°C. Thus, the temperatures of -5°C and less were the only regimes at which we could fabricate 15-20 nm wide trenches in gratings with 40-50 nm pitch. Examples of the highest resolution structures that we could obtain at various temperatures are given in Sect. 4. Another trend revealed by Fig.5 is that the cold development requires higher exposure doses, i.e. decreases the sensitivity of the process. Thus, the decrease in the development temperature from RT to -15°C in Fig. 5(a) has required an approximately 4 times higher line dose to obtain clearance of the resist.
To conclude, cold development results in a dramatic increase in the applicable dose window. However, this advantage is accompanied by a drop in the process sensitivity. Decreased temperatures therefore seem to be a preferred solution when maximizing the resolution is the priority.

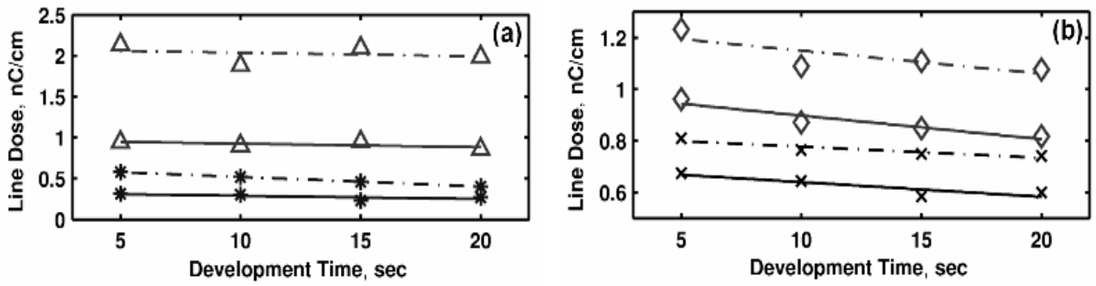

Fig. 5. The applicable dose windows for 70nm pitch (a) and 50nm pitch (b) gratings showing minimum (solid lines) and maximum (dashed lines) line doses for quality patterning. The symbols indicate the temperature of development: room temperature (stars), -5°C (crosses), and -15°C (triangles and diamonds) (adapted from Mohammad et al., 2009).

2.4 Low energy exposures require co-optimized development conditions

Our next target is to explore the EBL process when varying the energies of electrons from ultra low to moderate voltage regimes. Fig. 6 shows the examples of cross-sectional profiles for 70 nm pitch gratings fabricated with 3 keV, 10 keV, and 30 keV exposure energies. The grating exposed with 3 keV voltage shows pronounced undercuts because of strong forward scattering of the low-energy electrons (Lee et al., 1992). With increasing energy, the undercut decreases. 30 keV exposures produce almost straight interline walls.
Fig. 7 presents results of our analysis of the applicable dose windows when the exposure voltages of 3 keV, 10 keV, and 30 keV are employed to fabricate a 70 nm pitch grating. It can be seen that increasing the electron energy from 3 keV to 30 keV results in a dramatic increase of the dose windows. The reason of this is the decrease of the undercut when electrons' energy increases. The large applicable process window allows for more control over properties of the fabricated pattern, such as the aspect ratio. Thus, Figs. 8 demonstrates that in 70 nm gratings fabricated with 30 keV exposures, the variation of the line dose within the applicable window allows one to vary the width of the interline trenches from less than ~15 nm to 45 nm, and Fig. 9 shows the corresponding aspect ratio changes by a factor of two. The aspect ratio of PMMA walls turns out to be less sensitive to the change of the exposure dose because of a decrease of the wall height (see Fig. 8). However, according to

Fig. 7, the minimum applicable line doses increase roughly in proportion to the electron energy, resulting in a significantly lower sensitivity for 30 keV voltages. In contrast, 3 keV exposures provide a better sensitivity. Furthermore, strong undercuts that occur in the ultra-low energy processes may facilitate 3D shaping of the resist required for metallization and lift-off of high-resolution nanostructures, as will be demonstrated in Sect. 4. The complementary strengths of the low- and moderate-voltage exposures motivate further in-depth research of the corresponding process conditions.

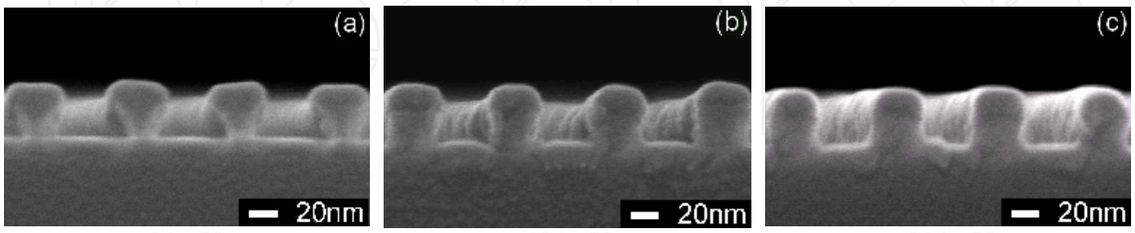

3 keV **10 keV** **30 keV**

Fig. 6. Cross sectional profiles in PMMA gratings exposed using various voltages.

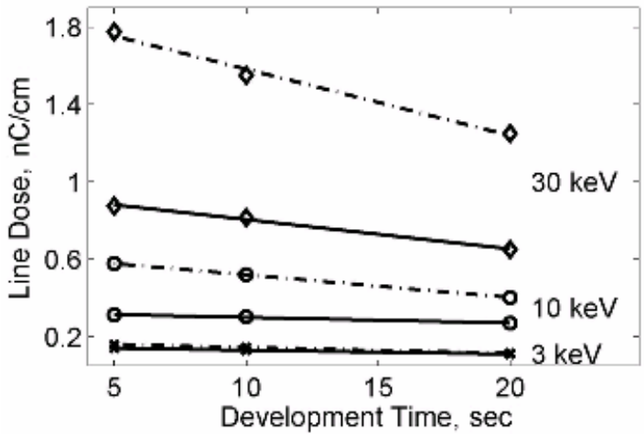

Fig. 7. Applicable dose windows for 70nm pitch gratings using the exposure voltages of 3 keV (crosses), 10 keV (circles), and 30 keV (diamonds). The samples were developed at RT, and the initial PMMA thickness was 55 nm. The meaning of the solid and dashed lines is as in Fig. 5.

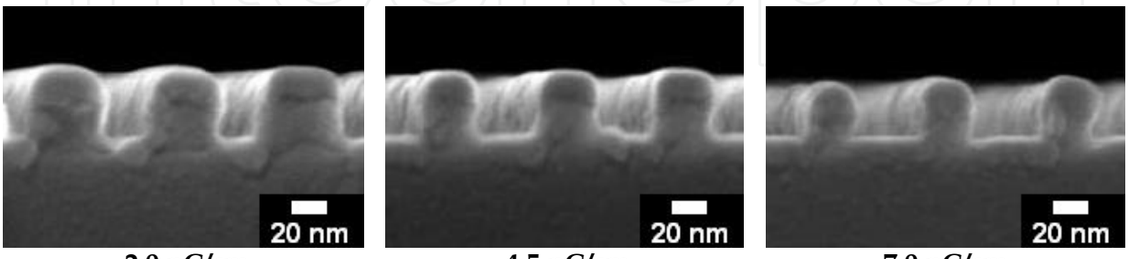

2.0 nC/cm **4.5 nC/cm** **7.0 nC/cm**

Fig. 8. Cross sectional profiles in 70 nm pitch PMMA gratings fabricated using 30 keV voltage and various line doses. The samples were developed at -15°C for 15 sec., and the initial PMMA thickness was 55 nm.

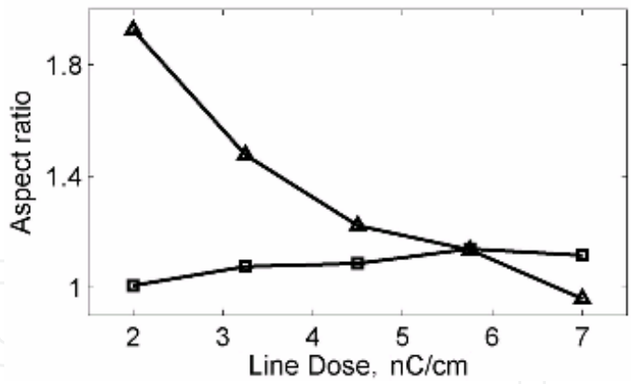

Fig. 9. Aspect ratios for the interline gaps (triangles) and PMMA lines (squares) as a function of the exposure dose, determined from cross-sectional SEM images for 70 nm pitch gratings fabricated using 30 keV electrons. Other process conditions were as in Fig. 8.

Tables 1 and 2 compare the process resolutions and sensitivities, expressed in terms of the applicable line dose boundaries d_{min} and d_{max}, for various exposure energies, development temperatures, and durations, when fabricating gratings with 70 nm and 50 nm pitches, respectively. From the table it is evident that obtaining reasonably broad dose windows with low energy exposures may require decreasing the development temperature, which

Voltage, develop. temperature, & initial resist thickness	Develop. time, sec.	Line doses, nC/cm			d_{max}/d_{min}
		d_{min}	d_{max}	$d_{max}-d_{min}$	
3 keV	5	0.135	0.155	0.020	1.15
RT	10	0.125	0.145	0.020	1.16
55 nm	20	0.110	0.115	0.005	1.05
3 keV	5	0.490	0.665	0.175	1.36
-15°C	10	0.460	0.630	0.170	1.37
55 nm	20	0.400	0.560	0.160	1.40
10 keV	5	0.313	0.578	0.265	1.85
RT	10	0.303	0.520	0.218	1.72
55 nm	20	0.270	0.403	0.133	1.49
10 keV	5	0.875	2.050	1.175	2.34
-15°C	10	0.870	2.040	1.170	2.34
55 nm	20	0.835	2.020	1.185	2.42
30 keV	5	0.875	1.775	0.900	2.03
RT	10	0.815	1.550	0.735	1.90
55 nm	20	0.650	1.250	0.600	1.92
30 keV	5	2.400	6.465	4.065	2.69
-15°C	10	2.400	6.250	3.850	2.60
55 nm	20	2.400	5.715	3.315	2.38

Table 1. The applicable line dose windows for 70 nm pitch gratings.

Voltage, develop. temperature, & initial resist thickness	Develop. time, sec.	Line doses, nC/cm			d_{max}/d_{min}
		d_{min}	d_{max}	$d_{max}-d_{min}$	
3 keV	5	0.370	0.430	0.060	1.16
-15°C	10	0.345	0.405	0.060	1.17
47 nm	20	0.295	0.350	0.055	1.19
10 keV	5	0.960	1.280	0.320	1.33
-15°C	10	0.940	1.260	0.320	1.34
55 nm	20	0.840	1.120	0.280	1.33
30 keV	5	0.750	1.040	0.290	1.39
RT	10	0.725	0.900	0.175	1.24
55 nm	20	0.600	0.695	0.095	1.16
30 keV	5	2.160	3.330	1.170	1.54
-15°C	10	2.200	3.210	1.010	1.46
55 nm	20	2.295	2.920	0.625	1.27

Table 2. The applicable line dose windows for 50 nm pitch gratings.

would however increase both the difference $d_{max}-d_{min}$ and the minimum applicable dose d_{min}. The implication is that using low-energy exposure regimes requires tradeoffs between the process resolution and sensitivity, which may be achieved by a careful co-optimising of the exposure voltage and development temperature. It is elucidative to compare the process employing 30 keV exposure and RT development with that using 3 keV exposures and -15°C. According to Tables 1 and 2, the ultra-low voltage exposure combined with cold development still leads to a strong improvement in the sensitivity. For both 70 nm and 50 nm pitches, the minimum applicable line dose d_{min} is approximately half for the 3 keV, cold development processes than for the 30 keV, RT ones. However, the applicable dose window $d_{max}-d_{min}$ is 2-5 times narrower for 3 keV than for 30 keV in the cases considered. One can conclude that, to profit from the improved sensitivity and 3D capacity with low voltage, cold development exposures, the applied dose should be chosen carefully in order to satisfy the relatively narrow requirements for quality fabrication.

One more control factor to be considered is the duration of development. In Tables 1 and 2 it can be seen that the minimum and maximum boundary doses d_{min} and d_{max} show a minor to moderate decrease with the development time in most cases, and so does the width of the applicable dose window $d_{max}-d_{min}$. In contrast, the ratio d_{max}/d_{min} is largely insensitive to the duration of development, although it depends on the voltage and grating pitch. Further discussion of these trends is given in Sect. 3.4. Noteworthy at this point is the fact that the optimum conditions for exposure (energy, dose) and development (temperature, time), are intimately interrelated and should be selected simultaneously for optimal performance of EBL at the nanoscale.

3. Theory and modelling insights into deep nanoscale-resolution EBL

As demonstrated in Sect. 2, both the exposure and development conditions should be selected carefully to reach the best quality of dense nanopatterns. In practice this may mean that 4 or even more process parameters must be co-optimized for a given resist-substrate-developer combination. To understand and systematize the relevant trends, predict the

outcomes, and potentially optimize EBL in-silico, appropriate numeric models should be employed and/or developed. Providing efficient theories and numeric models of the various stages of EBL can substantially facilitate the optimization at the nanoscale. Below we discuss some of the emerging challenges as well as our solutions for numeric modelling of the exposure and development stages of the EBL process.

3.1 Towards new modeling paradigm for exposures of positive resists

Electrons' travel and energy dissipation in resists is believed to be a well explored area of research. Hundreds of publications describing analytic and Monte-Carlo models for handling the interaction of electrons with resists might seem to address every aspect of this. The Reference list to this Chapter features just a few works (Kyser & Viswanathan, 1975; Murata et al., 1981; Lee et al., 1992; Raptis et al, 1993; Raptis et al, 2001; Zhou & Yang, 2006) out of a tremendous amount of literature on theory, modeling, and simulation of EBL exposures. However, the existing models of exposure are mostly limited to computations of the average amounts of energy deposited by primary, secondary, and backscattered electrons in the resist. The resulting distributions of deposited energy are then converted into the probability of bond scissions employing the so-called radiation chemical yield (G-factor), which is the number of main-chain scissions per 100 eV of deposited energy (Greeneich, 1974; Han et al., 2003; Kyser & Viswanathan, 1975). Usually, the G-factor is not

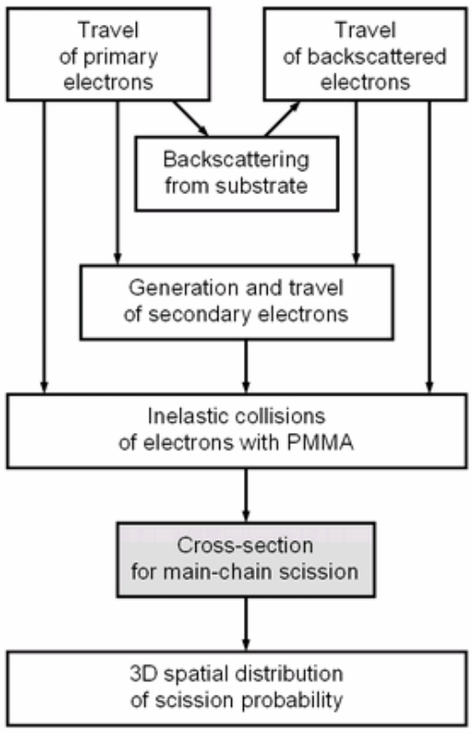

Fig. 10. Outline of our model for resist exposure in EBL. In the model, the probability of main-chain scissions is computed directly through the differential cross-section for inelastic collisions resulting in the scissions (Aktary et al., 2006). The model avoids uncertainties related with the conversion of the distributions of deposited energy into the number of main-chain scissions through the empirical radiation chemical yield.

known precisely and determined from experiments where the resist is exposed to extremely high-energy (1 Mev) electrons or gamma-rays (Chapiro, 1962). Use of such empirical G-factors involves a significant level of uncertainty, since the experimental conditions differ dramatically from those employed in EBL. We have also shown that the G-factor is not necessarily a constant, but may depend on the energies of electrons involved in collisions (Aktary et al., 2006), which should be accounted for. Furthermore, using the distributions of deposited energy as a starting point for the computations of the number of scissions is not an unequivocal choice, since a part of deposited energy is thermalized without scissions involved, whereas the actual yield of scissions is related intimately with the details of individual collisions of electrons with atoms of PMMA.

The uncertainties described above are avoided if one chooses an alternative approach employing a direct computation of the probability of main-chain scissions for each inelastic collision individually (Wu & Neureuther, 2001). By this, the conversion of the cumulative deposited energy into the number of scissions is avoided. We have recently introduced a model that explores this vision (Aktary et al., 2006), see also the outline in Fig. 10. In brief, after focused electrons hit a layer of PMMA on a substrate, they undergo both elastic and inelastic scattering in PMMA, as well as backscattering from the substrate. Travel of primary, secondary, and backscattered electrons in PMMA is described by transport theory, which provides a high robustness of the numerical algorithm. The model employs improved cross-sections for inelastic collisions, which were validated against the dielectric-response modeling (Tan et al., 2005). To account for scissions by the inelastic collisions, we compute the probability of dissociation of the main-chain C−C bonds employing a cross-section defined with an accounting for the molecular properties of PMMA's monomers such as the number of valence electrons and the dissociation energies of bonds. More details on the model are given elsewhere (Aktary et al., 2006). Fig. 11(a) shows an example of a computed 3D distribution of the probability of main-chain scissions in a periodic grating pattern.

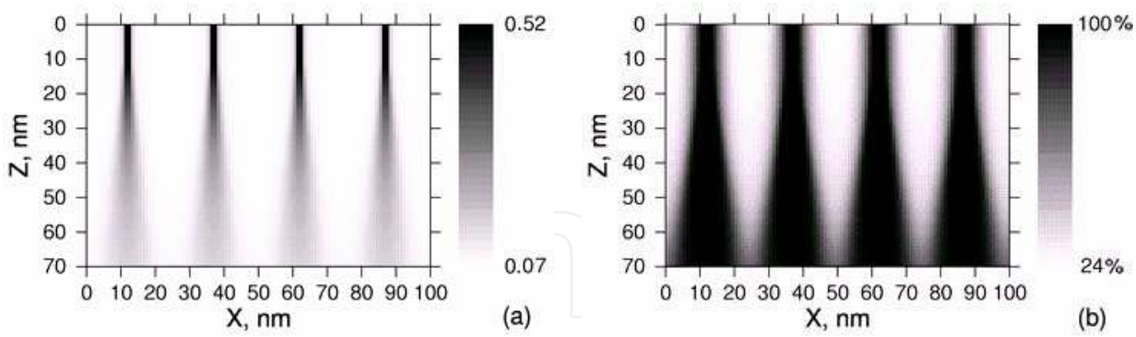

Fig. 11. Simulated probability of the main-chain scission per monomer of PMMA (a) and a corresponding volume fraction of small fragments, n≤12 (b), for a periodic grating with 25 nm pitch exposed with 10 keV electrons. The images present cross-sections of the 3D patterns, where Z is depth and X is width. Periodic boundary conditions were used in the horizontal directions, and Si substrate was located underneath the 70 nm layer of PMMA.

3.2 Fragmentation of PMMA and basic model of resist clearance

After the spatial distribution of the probability of chain scissions is computed, it is possible to identify the corresponding distribution of fragments of various weights. The distributions

of the various PMMA fragments are generally believed to be the major factor determining the outcome of the resist development, eventually defining the morphology of the clearance profiles. However, in spite of the understanding of this importance, molecular models of development and clearance were insufficiently addressed in the literature. Most available models of clearance of positive resists relate the distributions of deposited energy, or the corresponding probability of scission, with the local rate of development through various empirical coefficients (Greeneich, 1974; Han et al., 2003; Kyser & Viswanathan, 1975). Obviously, addressing ultra-high resolution processes at the deep nanoscale requires a more explicit accounting for the resist fragmentation to be included in the model. In our works, we have converted the computed 3D distribution of the probability of chain scissions into the spatial distribution of fragments of various weights employing the Poisson distribution (Aktary et al., 2006; Mohammad et al., 2007) or the geometrical distribution (Fito et al., 2009). As the next step, we assume as a tentative approximation that fragments with molecular weight less than a maximum number of monomers, n_{max}, are preferentially soluble at the development stage and thus responsible for the resulting morphology of the resist. This allows dichotomizing the spatial distributions of PMMA fragments into a light and preferentially soluble fraction ($n \leq n_{max}$) and a heavier and less soluble fraction ($n > n_{max}$). Fig. 11(b) shows an example of a spatial distribution of the volume fraction of small fragments for an example of n_{max}=12.

It is clear that the overall volume fraction of small fragments in the resist increases with the exposure dose, and the fraction of the heavier fragments decreases accordingly. This is demonstrated by Fig. 12, which shows the maximum percentage of the heavy fraction ($n > n_{max}$), encountered in a dense grating pattern as a function of the area dose, for the various values of n_{max}. It can be seen that the dependencies have a sharp step, whose position depends on n_{max}. It worth to note a qualitative resemblance of the dependencies in Fig. 12 with experimentally measured contrast curves representing the dependence of the remaining resist on the dose (Hasko et al, 2000; Yan et al., 2008). This resemblance implies that the conditions of clearance are intimately related with the size distribution of fragments in the exposed resist. In particular, it is reasonable to hypothesize that during development, PMMA is removed at locations where the content of small, preferentially soluble fragments exceeds a given threshold value C_{min} (Aktary et al., 2006). With this assumption, it is possible to convert spatial distributions of the light fraction of PMMA into 3D profiles of

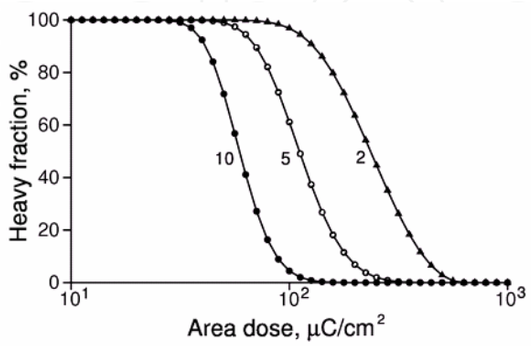

Fig. 12. The maximum percentage of volume fraction of the heavier, less soluble fraction ($n > n_{max}$), in a dense grating pattern as a function of the exposure dose, for the examples of n_{max}= 2, 5, and 10 monomers (adapted from Aktary et al., 2006).

clearance, provided that the parameters n_{max} and C_{min} are available. Fig. 13 presents examples of the clearance profiles for a periodic grating structure exposed with various doses, for the assumed values n_{max}=12 and C_{min}=90% (Mohammad et al., 2007).
With the computed clearance profilers, it is possible to analyze the regimes of clearance as a function of the process conditions. Thus for gratings, the regimes of underexposure (insufficient clearance) and overexposure (excessive clearance) are immediately available from the simulated clearance profiles as demonstrated in Fig. 13.

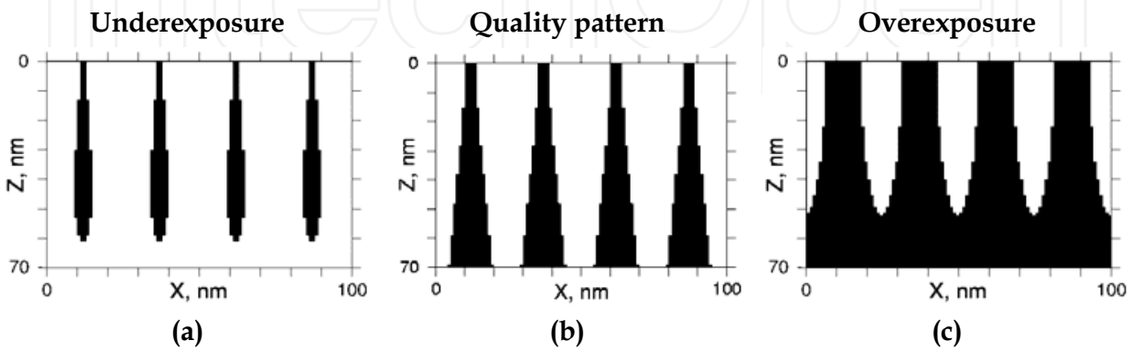

Fig. 13. Simulated clearance regimes for gratings in 70nm thick PMMA exposed by 10 keV electrons with various doses. Black – no resist; white – resist (Mohammad et al., 2007).

In Fig. 4 (Sect. 2.2.) the numerically determined boundary doses for underexposure and overexposure in various gratings are compared with the experiment. The clearance model parameters were as in Figs. 11 and 13. The lower curve in Fig. 4 (open triangles) represents the minimum area dose required for clearance of lines over their entire depth. This dose decreases roughly in proportion to the inverse of the grating period as discussed in Sect. 2.2. The upper curve (open diamonds) shows the boundary dose for overexposure, at which neighbor lines start merging. Since the neighbor lines overlap is less for larger interline distances, higher doses are required to clear the walls between the lines and therefore the boundary dose for overexposure increases with the grating pitch. The overall agreement between the numerical results and experimentally determined boundary doses for underexposure and overexposure is reasonably good, indicating that these limiting factors are well captured by the fragmentation-based model of clearance.
From Fig. 4 it is evident that the theoretical limit of resolution for gratings fabricated in PMMA with a 65 nm initial thickness is close to a 20 nm pitch. It is also possible to identify the area dose at which the best resolution can be reached (which is close to 80 μC/cm² in this case). However, it is also evident that the clearance conditions alone are insufficient to describe the quality of dense nanostructures. The pattern degradation, such as micellization or collapse, may occur at lower doses than over-clearance. As a result, the dose windows determined experimentally are narrower and the actual process resolution is lesser than predicted by the basic model of clearance. Thus, the predicted resolution can be considered as an ultimate theoretical limit, which would only be attainable if resist degradation during development is avoided.
Since the fragmentation-based model of clearance is representative of trends determined by the exposure, it may be useful to analyse the dependence of the EBL process on the applied voltage. Fig. 14 presents the computed boundaries for underexposure and overexposure in

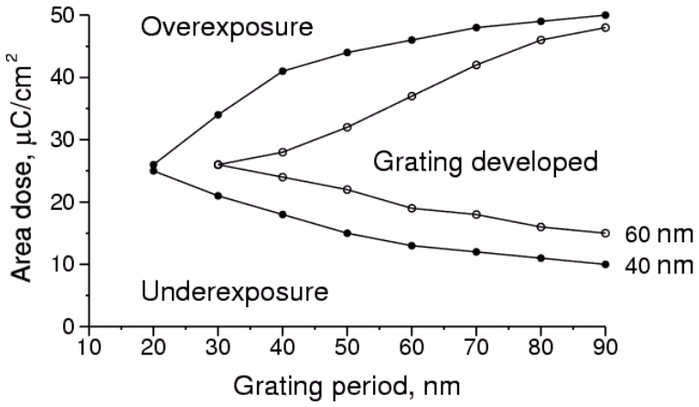

Fig. 14. Simulated clearance regimes for 3 keV exposures of gratings in PMMA with the initial thickness of 60nm (open circles) and 40nm (filled circles), (Stepanova et al., 2007).

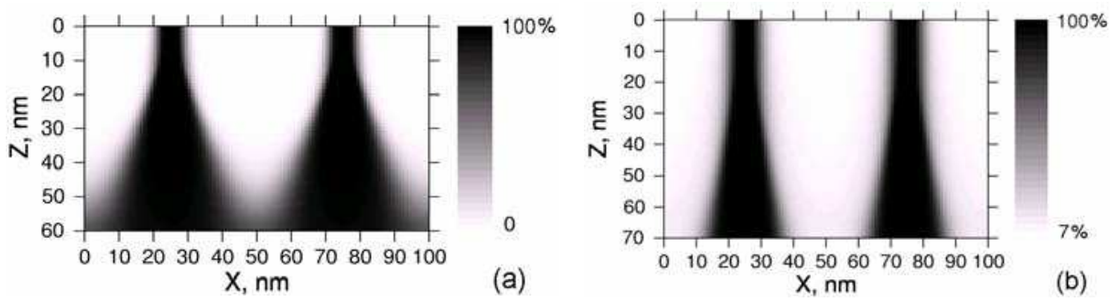

Fig. 15. Simulated distributions of light PMMA fraction (1 to 12 monomers) for a grating with 50 nm pitch, for the exposure voltages of 3 keV and (a) and 10 keV (b). The area doses correspond to the best theoretical resolution as defined from Figs. 14 and 4, i.e. 27 μC/cm² and 75 μC/cm², respectively (adapted from Stepanova et al., 2007).

gratings for 3 keV electrons energy. It can be seen that the predicted dose windows for 60 nm thick PMMA are dramatically narrower in comparison with modeling results for 10 keV exposures shown in Fig. 4, and the resolution limit is shifted toward sparser gratings. Thus, the theoretical dose window for 50 nm gratings in 60 nm thick PMMA is 10 times narrower for 3 keV exposures than for 10 keV exposures. The origin of this is clarified by Figs. 15 (a) and (b) which compare the spatial distributions of the light PMMA fraction in a periodic grating structure exposed by 3 keV and 10 keV electrons, respectively. It can be seen that the distribution for 3 keV broadens from the top down significantly more than that for 10 keV. The evident explanation is the strong forward scattering of the low-energy electrons. The corresponding broadening of the intensely exposed area leads to the undercuts in the clearance profiles, which is also confirmed by the experiment in Fig. 6(a). As a result the neighbour lines' overlap increases, which limits the resolution. However, a thinner (40 nm) resist layer allows fabrication of smaller features, as well as offers a wider window of favourable doses for high-resolution writing. The reason is that the broadening by forward scattering strongly increases with the depth (see Fig. 15(a)), so that the overlap is less pronounced at lower thickness of the resist. Another trend evident from the comparison of the numerical results in Figs. 4 and 14 is that the predicted area dose for optimum resolution is approximately three times less for 3keV exposures than for 10 keV exposures.

One can conclude that the basic model of clearance represents reasonably the dependencies of the EBL process on the conditions of exposure, such as the applied dose and voltage. Qualitatively, the model predictions are in agreement with the experimentally observed bahaviour of the overall resist clearance on the dose (contrast curves), as well as with the dependencies of the resolution and sensitivity on the conditions of exposure for dense high-resolution nanopatterns. Some of these trends can be predicted quantitatively. For example, the regimes of clearance in dense nanopatterns or the voltage dependence of the optimum area dose for the best resolution (see Figs. 4, 14, and 6). However, the model includes parameters n_{max} and C_{min}, which are not known precisely. Various resists, developers, and development conditions (such as temperature) would generally require a different parameterization. Also this framework does not address explicitly the kinetics of the development, as well as the limiting factors originating from the resist degradation, such as collapse. To extend the capacity of modeling toward a more detailed interpretation of the experimentally observed trends, and efficiently optimize the various aspects of post-exposure stages of EBL, a complementary kinetic analysis of the resist dissolution is required as outlined in the next section.

3.3 On the kinetics of resist dissolution

To analyse kinetics of resist dissolution, we have adopted as a background the mean-field model of diffusion in polymeric systems introduced recently (Scheinhardt-Engels et al., 2003). The model accounts for the molecular mobility, intermolecular interactions, and pressure relaxation in a system containing a solvent and polymer chains of a given length. In contrast to the original work (Scheinhardt-Engels et al., 2003), which addresses only the stationary-state boundary conditions, we have considered a more general case by adopting non-stationary behaviours. This generalization, however, does not affect the basic equations which are similar to those given in (Scheinhardt-Engels et al., 2003), and read:

$$\frac{\partial \varphi_A(\mathbf{r},t)}{\partial t} = -\nabla \mathbf{J}_A(\mathbf{r},t); \tag{1}$$

$$\mathbf{J}_A(\mathbf{r},t) = -\frac{D_A \varphi_A(\mathbf{r},t)}{\sum_C D_C \varphi_C(\mathbf{r},t)} \sum_B D_B \varphi_B \nabla\left(\mu_A(\mathbf{r},t) - \mu_B(\mathbf{r},t)\right); \tag{2}$$

$$\nabla \mu_A(\mathbf{r},t) = \sum_B \left(\frac{\delta_{AB}}{\varphi_A(\mathbf{r},t) N_A} - \frac{1}{N_B} + \chi_{AB} - \sum_C \varphi_C(\mathbf{r},t) \chi_{BC} \right) \nabla \varphi_B(\mathbf{r},t); \tag{3}$$

$$\sum_A \varphi_A(\mathbf{r},t) = 1. \tag{4}$$

Here A, B, and C denote the molecules type, i.e. the polymer (PMMA) fragments of various size and the developer; N_A is the number of segments (e.g. monomers) in molecule A; $\varphi_A(\mathbf{r},t)$ is the volume fraction of the component A as a function of the location $\mathbf{r}$ and time t; $\mathbf{J}_A$ is the flux of the component A; $\nabla\mu_A$ is the local gradient of the chemical potential driving the kinetic process expressed by the flux $\mathbf{J}_A$; χ_{AB} is the Flory-Huggins (FH) interaction parameter, D_A is the diffusivity, and δ_{AB} is the Kronecker delta function.

With appropriate initial and boundary conditions, the numeric solution of Eqs. (1-4) would predict spatial re-distribution of the components as functions of time *t*. This, however, would require defining the FH interaction parameters χ_{AB} and the diffusivities D_A for all components in the system, which is a very complex task. Also the numeric solution of the full system of equations in the multicomponent mixture is a relatively time-consuming process, whereas a high numeric efficiency is required for a model that could potentially be employed for in-silico aided optimization of EBL process. For these reasons, we have employed the system of equations (1-4) as a starting point to derive a simpler, but more efficient *ansatz* that describes the kinetic process of development by the movement of the resist-developer interface, and contains less unknown parameters than Eqs. (1-4).

To derive our approximate model of resist dissolution (Fito et al., 2009), we consider PMMA embedded in a developer (solvent). PMMA may contain fragments of various sizes (numbers of monomers) n=1, 2, 3, … . However, at every location **r** the polymer melt is represented by one characteristic size of fragments (this may be a monodisperse polymer or a polydisperse system represented by local average fragment size). We denote the developer and PMMA fragments by indexes 0 and i, respectively, and assume that the diffusivity of the developer is higher than the diffusivity of PMMA, $D_0 >> D_i(\mathbf{r})$. Further, we define the position of the resist-developer interface, $\mathbf{r}_{int}$, as the level surface of equal developer concentration, $\varphi_0(\mathbf{r}_{int},t) = p = \text{constant}$, such that $1 - \varphi_0 << 1$ at the interface. Next, we introduce the velocity at which the interface changes its position, $\mathbf{v}=d\mathbf{r}_{int}/dt$, and which is determined by the flux of the developer at the interface,

$$\mathbf{v}\cdot\nabla\varphi_0\big|_{\mathbf{r}=\mathbf{r}_{int}(t)} = \nabla\mathbf{J}_0\big|_{\mathbf{r}=\mathbf{r}_{int}(t)}. \tag{5}$$

Depending on the sign of $\nabla\mathbf{J}_0$ one can distinguish two regimes: prevailing swelling ($\nabla\mathbf{J}_0>0$), and prevailing shrinking ($\nabla\mathbf{J}_0<0$). Considering that swelling of the resist occurs only at the beginning of dissolution, whereas shrinking is the major mechanism responsible for development, we have focused our analysis on the shrinking regime. With these definitions and assumptions, we have obtained the following expression for the velocity of motion of the resist-developer interface (Fito et al., 2009):

$$v = \eta D_i(\mathbf{r}_{int})L^{-1}. \tag{6}$$

In Eq. 6, $D_i(\mathbf{r}_{int})$ is the diffusivity of PMMA at the location $\mathbf{r}_{int}$ and η is a constant coefficient that depends on the function $\varphi_0(\mathbf{r})$ near the interface. For example if the function φ_0 decays asymptotically as $\varphi_0 \sim x^{-1}$, where x is the penetration depth of the developer into the resist, the coefficient is $\eta = 2(1-p)(1-2\chi)$, where χ is the FH parameter describing the interaction of developer with PMMA such that $1-2\chi \geq 0$. L in Eq. 6 is the depth or shrinking of the resist. From Eq. 6, the following expression follows that describes the kinetics of resist shrinking:

$$\frac{dL}{dt} = \tilde{D}_i(\mathbf{r}_{int})L^{-1}, \tag{7}$$

where $\tilde{D}_i$ is the effective diffusivity, $\tilde{D}_i = \eta D_i$. In the case of constant diffusivity D_i, the integration of Eq. 7 leads to the well-known expression for the diffusion length, $L\sim(D_i t)^{1/2}$. For the corresponding rate of resist dissolution, one obtain the relation $v\sim(D_i/t)^{1/2}$.

The important implication of Eqs. 6 and 7 is that the rate of resist dissolution is a function of the entire history of the process of development, and thus depends on development time explicitly. This is different from the framework adopted in most if not all available models of EBL resist development, which assume the existence of a stationary regime that can be described by a constant rate of dissolution (Greeneich, 1974; Han et al., 2003; Hasko et al., 2000). Our analysis demonstrates that this assumption is not applicable in general, and that a more complex kinetics of dissolution, e.g. such as expressed by Eq. 7, should be accounted for to describe resist development at the nanoscale.

Employing Eq. 7, we have implemented an efficient finite-element numeric algorithm to model the process of development of exposed PMMA. As the initial condition, we use our computed 3D distributions of the probability of scission in the resist (see e.g. the example in Fig. 11(a)). We convert the local probability of scission into the local volume fractions of PMMA fragments of various size $\varphi_n(x,y,z)$, where n = 1, 2, 3, … is the number of monomers in a fragment. For the normalized diffusivity of fragments of size n, we employ the following expression (Masaro & Zhu, 1999; Miller-Chou & Koenig, 2003),

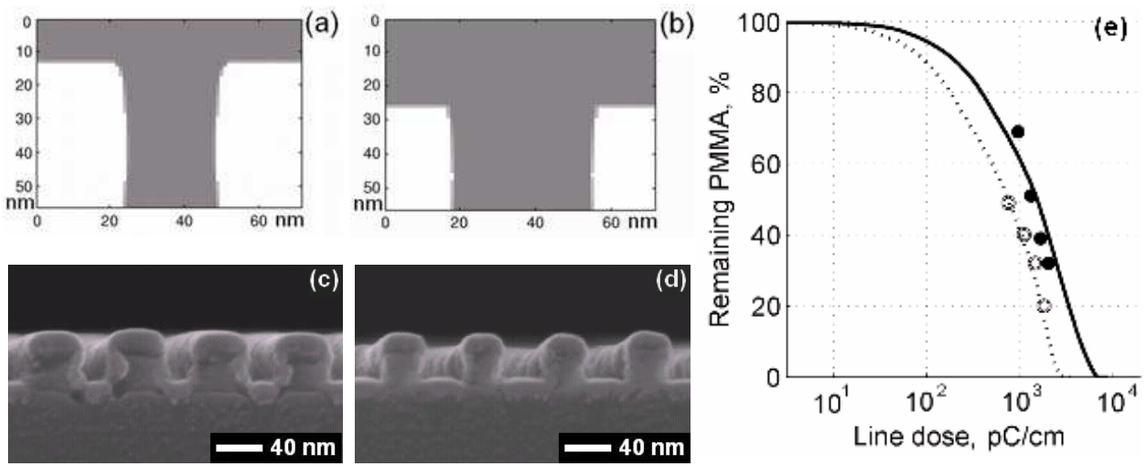

Fig. 16. (a,b) – computed cross-sectional profiles (white - PMMA, grey – no PMMA) in a periodic 70 nm pitch grating exposed by 10 keV electrons with the doses of 700 pC/cm and 1300 pC/cm, respectively, and developed at -10°C during 20 sec; (c,d) – SEM cross-sectional profiles for similar conditions; (e) – computed (lines) and experimental (symbols) percentages of remaining PMMA as functions of the exposure dose, in a 70 nm pitch grating exposed by 10 keV electrons and developed at -15°C during 5 sec. (solid line and filled symbols) and 20 sec. (dotted line and open symbols), (adapted from Fito et al., 2009).

$$\tilde{D}_n = a\, n^{-\alpha} \exp(-U/kT), \tag{8}$$

where a and α are model parameters, U is the activation energy, and T is temperature. In polydisperse polymers melts, the proportionality $\tilde{D}_n \sim n^{-\alpha}$ can be interpreted as describing the mobility of molecules of size n in a media which properties are represented by power α. Obviously, the mobility decreases with the size of molecules, i.e. smaller molecules are more mobile than larger ones. Since in exposed resist the fragment sizes are represented by the distribution φ_n, a location-dependent average effective diffusivity D can be introduced,

$$D(x,y,z) = \left\langle \widetilde{D}_n \right\rangle = \left\langle \frac{\beta}{n^{\alpha(x,y,z)}} \right\rangle, \tag{9}$$

where the averaging is performed over the local distribution of fragments, and $\beta = a \cdot \exp(-U/kT)$. In most polymers, the power α varies from 1 in dilute solutions of small molecules to 2 or even higher for denser melts of longer polymer chains, where the mobility is dampened by entanglement (Harmandaris et al., 2003; Masaro & Zhu, 1999; Miller-Chou & Koenig, 2003). We have employed the following dependence for α,

$$\alpha(x,y,z) = \begin{cases} 1 + \langle n \rangle / \gamma, & \langle n \rangle < \gamma; \\ 2, & \langle n \rangle \geq \gamma. \end{cases} \tag{10}$$

We simulate the process of development by a sequence of discrete dissolution steps, where time δt required to dissolve a resist layer of thickness δL is determined by $\delta t = 2L\delta L / D(x,y,z)$. The simulation provides the location of the 3D resist-developer interface as a function of time. The parameters β and γ can be evaluated by fitting the computed percentages of PMMA left on the substrate to the corresponding experimental results. We obtain these from the SEM cross-sectional profiles for gratings, and parameterize our model by minimizing the mean square difference using the simulated annealing algorithm (Fito et al., 2009). It has been assumed that the parameters β and γ may depend on temperature of development, but not on other process conditions.

Fig. 16 presents our computed cross-sectional clearance profiles for a 70 nm pitch grating (a,b) and the amount of remaining PMMA (e) in comparison with the corresponding experiments. The fit model parameters that we employed in these examples were: Fig. 16(a,b) – $\beta = 2.34 \cdot 10^3$ nm^2/s, $\gamma = 23.1$; Fig. 16(e) – $\beta = 2.38 \cdot 10^3$ nm^2/s, $\gamma = 16.5$ (Fito et al., 2009). From Fig. 16 it can be seen that the kinetic model describes quite well the broadening of the clearance trenches in gratings, the thinning of the walls, as well as the shrinkage of the thickness of the resist during development. The dependencies of the total amount of PMMA remaining at the substrate on the exposure dose and development time are also represented with a promising accuracy. However, this simple model does not capture all the details of the shape the cross-sectional profiles, which appear to be smoother at the top, and show stronger undercuts at the base, than predicted numerically. We expect that some of these differences may originate from surface tension forces and/or plastic deformation; the potential impact of these factors still needs to be investigated.

3.4 Kinetic model for applicable dose windows

In this section we extend our kinetic modeling framework to describe the boundary exposure doses for the conditions of resist underexposure and collapse, d_{min} and d_{max}, which determine the applicable dose windows and by this represent the nanoscale resolution and sensitivity of EBL (see Sect. 2).

Our numerical results presented in Figs. 16 (a,b) demonstrate that at a given development time, the locations at which the resist clearance occurs depend on the exposure dose. At lesser doses PMMA is removed preferentially from the intensely exposed trenches where fragments are the most mobile (see Fig. 16(a)), whereas more intense exposures allow for partial dissolution of interline walls containing heavier, less mobile fragments (Fig. 16(b)). According to the kinetic model described in Sect. 3.3, dissolution of the exposed PMMA can

be described as a kinetic diffusion-like process, with the effective diffusivities of fragments represented by Eq. 8. For simplicity, we now describe the average local diffusivity in terms of the mean number of monomers in fragments ⟨n⟩, $D \sim \langle n \rangle^{-\alpha}$ (Masaro & Zhu, 1999). For moderate exposure doses, ⟨n⟩ is inversely proportional to the local probability of scissions (Aktary et al., 2006), which in turn is proportional to the applied dose d. The dose dependence can therefore be approximately accounted for by $\langle n \rangle \sim 1/d$. As a result, the average diffusivity of fragments in exposed PMMA becomes

$$D = c d^{\alpha} \exp(-U/kT), \tag{11}$$

where c and α are, in general, location-dependent parameters. In our recent work (Mohammad et al., 2009) we have assumed that for a given development time and pattern geometry, the minimum and maximum applicable doses for quality nanofabrication, d_{min} and d_{max}, correspond to the same value of the average diffusivity D in the exposed trenches and in the walls, respectively. This assumption results in the following equation for the temperature dependence of these boundary exposure doses d_{min} and d_{max} for a given development time and pattern geometry:

$$d_{\substack{min,\\max}} = d^{ref}_{\substack{min,\\max}} \exp\left(\frac{U}{\alpha_{\substack{min,\\max}} k} (1/T - 1/T^{ref}) \right). \tag{12}$$

Here 'ref' denotes a reference value of the minimum or maximum applicable dose and of the development temperature, and the notation $\alpha_{min,max}$ indicates that the dependencies for d_{min} and d_{max} may correspond to different α values. Here, however, we use a single value U/α=0.22eV, which we evaluated empirically (Mohammad et al., 2009). In Fig 17, we compare the corresponding theoretical results with the experimental temperature dependencies for the boundary line doses in a 70 nm pitch grating exposed with 10 keV electrons. We used the experiments for -15°C for reference.

As it can be seen in Fig. 17, Eq. 12 describes very well the broadening of the applicable dose window with the decrease of the development temperature that we have observed experimentally. According to the model assumptions, the lower boundary of the applicable dose window d_{min} can be interpreted as the dose at which PMMA fragments in the intensely exposed trenches are mobile enough to be removed over the time of development. The maximum applicable dose d_{max} is, in turn, determined by molecular diffusion processes occurring in the walls. The applicable dose window d_{max}–d_{min} is therefore defined by the difference in these diffusivities. It is noteworthy that, if the parameter α is a constant ($\alpha_{min}=\alpha_{max}$), Eq. 12 predicts that the decrease in temperature would increase the difference d_{max}–d_{min}, but not the ratio d_{max}/d_{min}. This prediction is very well confirmed by our experiments for 50 nm pitch gratings exposed with 30 keV electrons (Table 2). For 70 nm pitches (Table 1) we observe a moderate temperature dependence of d_{max}/d_{min}; however the reasonable agreement of the theory with experiment in Fig. 17 seems to confirm the viability of the approximate model. Further development of the kinetic framework, which is currently in progress, will provide more detailed predictions for the sensitivity and resolution of EBL.

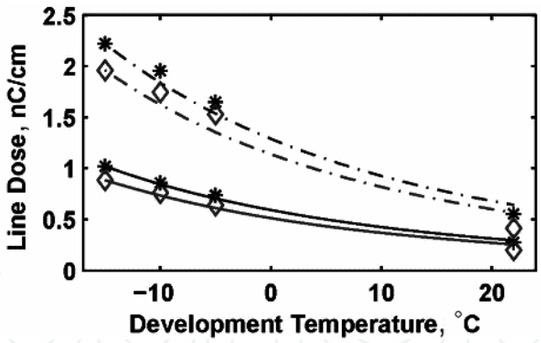

Fig. 17. Comparison of theoretical temperature dependencies for minimum (solid lines) and maximum (dashed lines) applicable exposure doses for a 70 nm pitch grating exposed with 10 keV electrons. The symbols show the experimental data for development times of 5 sec. (stars) and 20 sec. (diamonds) (adapted from Mohammad et al., 2009).

4. The perspective of low-voltage EBL process optimization

From the previous discussion it is evident that fabricating dense nanopatterns with specified characteristics is a complex optimisation task. At least 4 process parameters (the exposure voltage, dose, development temperature, and time) must be co-optimized for a given resist-substrate-developer combination. Our approach comprises a thorough experimental study as well as numerical analysis that allow interpreting and systematising the observed trends. In Sect. 2 we have described the major limiting factors for nanoscale resolution in EBL (underexposure and collapse) and employed the corresponding window of applicable exposure doses as a descriptor for the dependence of resolution and sensitivity on the various process conditions. Based on this framework, we obtained extensive experimental benchmarks representing the dependencies of the boundary doses d_{min} and d_{max} as functions of the size of nanostructures, development time, and temperature. Employing the suite of numeric models described in Sect. 3 has facilitated understanding of the observed trends and allowed us to develop an efficient methodology for optimizing the EBL process at the nanoscale.

The examples in Fig. 18 show the highest resolution grating structures that we obtained by exposing 47-55 nm thick layers of PMMA to 10 keV electrons, for various development temperatures. Thus RT development yields 33 ± 2 nm wide trench lines in a grating with a 70 nm pitch (Fig. 18(a)). With -10 °C development, we could fabricate 20 ± 2 nm lines in a 50 nm pitch grating (Fig. 18(b)). This line width was further improved to 15 ± 2 nm in a 40 nm pitch grating at -15°C temperature (Fig. 18(c)). One can conclude that the minimal resolved feature size significantly decreases with decrease of the development temperature from RT down to -15°C. This is consistent with the observed trend of broadening of the applicable dose windows, and explained by the kinetics of fragment mobility during resist dissolution.

3 keV exposures provide a significantly higher throughput than 10 keV ones, which is accompanied by narrower process windows because of large undercuts of the resist (see Sect. 2.4 and 3.2). However, despite the limitations in resolution of low-voltage EBL, the undercuts facilitate metallization and lift-off for ultrahigh-resolution processes. By combining 3 keV voltage exposures with cold development, we were able to fabricate highly uniform arrays of 20 nm wide metal (Cr) lines in a grating configuration with a 60 nm pitch, such as shown in Fig. 19. The cold development enabled a sufficient robustness of the

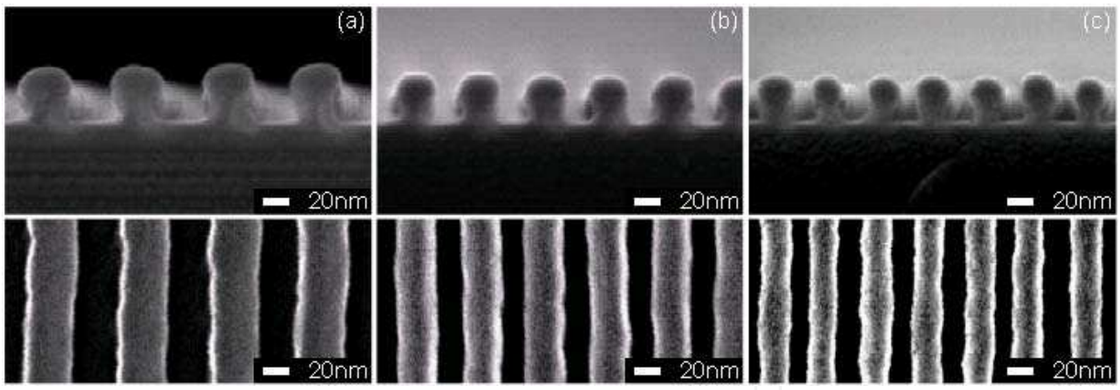

Fig. 18. Cross-section and top-view micrographs showing examples of optimized dense nanoscale gratings fabricated in PMMA using a Raith 150 system with 10keV voltage, and employing various development temperatures: (a) RT, 70nm pitch; (b) - 10 °C, 50nm pitch; and (c) - 15°C, 40nm pitch (Mohammad et al., 2009).

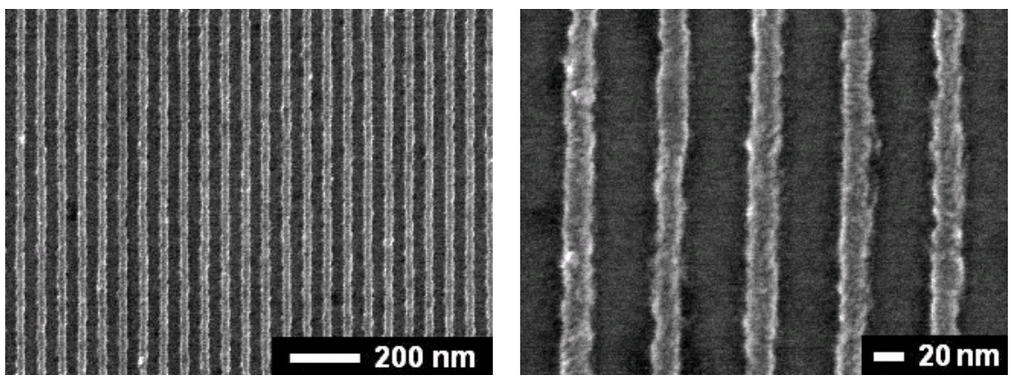

Fig. 19. 20 nm-wide Cr lines in a 60 nm pitch grating, fabricated by 3 keV exposure of a single layer of PMMA-950K, and developed at -15°C. Evaporation of a ~15 nm thick Cr layer was employed followed by ultrasonic lift-off. The substrate is a layer of SiCN on a Si wafer.

process, whereas the undercuts created by the ultra-low energy exposures allowed us to use a single layer of PMMA-950. Overall, the low-voltage based process turned out to be significantly more efficient than the conventional bi-layer schemes that are often used for lift-off at the deep nanoscale.

5. Conclusion

We have studied systematically the resolution and sensitivity of EBL processes for moderate to ultra low voltage exposures. We have employed the conventional resist (PMMA) and developer (MIBK:IPA mixture), however, we have varied the development temperature from RT down to -15°C. We consistently observe that the lowest development temperatures yield the largest applicable dose windows, but also require the highest clearance doses.
Our results indicate that both moderate and low voltage exposures offer great potential for efficient fabrication at the nanoscale dimensions. However, for reaching the ultimate resolution with ultra-low energy exposures, both the exposure and development conditions should be considered as interdependent factors and optimized simultaneously. The major

research challenge is related to the molecular mechanisms of development, which should be understood thoroughly in order to efficiently optimize low-voltage EBL.
We have suggested an improved framework for modeling fragmentation of positive resists, and also described a suite of models for clearance. These models have proven to be extremely useful for understanding and systematising the observed trends. Furthermore, the described models of resist development offer a strong potential for in-silico optimization of EBL. Further effort should address the diverse physico-chemical processes accompanying the resist dissolution, such as gelation, swelling, surface tension, and plastic deformation, whose potential impact on the resolution is not yet understood sufficiently. For strengthening the predictive capacity of the kinetic models, their parameterization employing more detailed molecular simulations should also be implemented.

6. Acknowledgements

The authors thank Marko van Dalfsen for his assistance with the EBL process, and Zsolt Szabó for designing dose test samples and his programming contributions. The work was supported by NINT-NRC, NSERC, Alberta Ingenuity, iCORE, and Raith GmbH.

7. References

Aktary, M., Stepanova, M., & Dew, S.K. (2006) Simulation of the spatial distribution and molecular weight of PMMA fragments in electron beam lithography exposures. *J. Vac. Sci. & Technol. B*, Vol. 24, pp. 768-779.

Brünger, W., Kley, E.B., Schnabel, B., Stolberg, I., Zierbock, M., & Plontke, M. (1995) Low energy lithography; Energy control and variable energy exposure. *Microelectronic Engineering*. Vol. 27, pp. 135-138.

Chapiro, A. (1962) *Radiation Chemistry of Polymeric Systems,* Wiley, ISBN 0470392851, New York, p. 515.

Cord, B., Lutkenhaus, J. & Berggren, K.K. (2007) Optimal temperature for development of polymethylmethacrylate. *J.Vac. Sci. & Technol. B.,* Vol. 25, pp. 2013-2016.

Dial, O., Cheng, C.C. & Sherer, A. (1998) Fabrication of high-density nanostructures by electron beam lithography. *J.Vac. Sci. & Technol. B.,* Vol. 16, pp. 3887-3890.

Fito, T., Mohammad, M.A., Szabó, Zs., Chen, J., Aktary, M., & Dew, S.K., & Stepanova, M. (2009) *manuscript in preparation.*

Greeneich, J.S. (1974) Time evolution of development contours in poly-methylmethacrylate electron resist. *J.Vac. Sci. & Technol.* Vol. 12, pp. 5264-5268.

Häffner, M., Heeren, A., Fleischer, M., Kern, D.P., Schmidt, G., & Molenkamp, L.W. (2007) *Microelectronic Engineering*. Vol. 84, pp. 937-939.

Harmandaris, V.A., Mavrantzas, V.G., Theodorou, D.N., Kröger, M., Ramírez, J., Öttinger, H.C., & Vlassopoulos, D. (2003) Dynamic crossover from Rouse to the entangled polymer melt regime: Signals from long, detailed atomistic molecular dynamics simulations, supported by rheological experiments. *Macromolecules,* Vol. 36, pp. 1376-1387.

Hasko, D.G., Yasin, S. & Mumatz, A. (2000) Influence of developer and development conditions on the behaviour of high molecular weight electron beam resists. *J.Vac. Sci. & Technol. B.* Vol. 18, pp. 3441-3444.

Han, G., Khan, M., & Cerrina, F. (2003) Stochastic modeling of high energy lithographies. *J.Vac. Sci. & Technol. B.,* Vol. 21, pp. 3166-3171.

Jamieson, A., Wlson, C.G., Hsu, Y. & Brodie, A.D. (2004) Low-voltage electron beam lithography resist processes: top surface imaging and hydrogen silisesquioxane bilayer. *J. Microlith., Microfab., Microsyst*. Vol. 3, pp. 442-449.

Kyser, D.K. & Viswanathan, N.S. (1975) Monte Carlo simulation of spatially distributed beams in electron-beam lithography. *J.Vac. Sci. & Technol.* Vol. 12, pp. 1305-1308.

Lee, Y. H., Browing, R., Maluf, N. , Owen, G. & Pease, R.F.W. (1992) Low voltage alternative for electron beam lithography. *J.Vac. Sci. & Technol. B.* Vol. 10, pp. 3094-3098.

Liddle J.A., Gallatin, G.M. & Ocola, L.E., (2003) Resist requirements and limitations for nanoscale electron-beam patterning. *Mat. Res. Soc. Symp.Proc.*Vol.739, pp. H1.5.1-12.

Masaro, L. & Zhu, X.X. Physical models of diffusion for polymer solutions, gels and solids. (1999) *Prog. Polym. Sci*. Vol. 24, pp. 731-775.

Miller-Chou, B.A., Koenig, J.L. (2003) A review of polymer dissolution. *Prog. Polym. Sci*. Vol. 28, pp. 1223-1270.

Mohammad, M.A., Dew, S.K., Westra, K., Li, P. Aktary, M., Lauw, Y., Kovalenko, A., & Stepanova, M. (2007) Nanoscale resist morphologies of dense gratings using electron-beam lithography. *J.Vac. Sci. & Technol. B,* Vol. 25, pp. 745–753.

Mohammad, M.A., Fito, T., Chen, J., Aktary, M., Stepanova, M., & Dew, S.K. (2009) Interdependence of optimum exposure dose regimes and kinetics of resist dissolution for electron-beam nanolithography of PMMA. *J. Vac. Sci. Technol. B. In press*.

Murata, K., Kyser, D.F. & Ting, C.H. (1981) Monte Carlo simulation of fast secondary electron production in electron beam resists. *J.Vac. Sci. & Technol.,* Vol. 52, pp. 4396-4405.

Ocola L.E. & Stein A. (2006) Effect of cold development on improvement in electron-beam nanopatterning resolution and line roughness. *J.Vac. Sci. & Technol. B.,* Vol. 24, pp. 3061-3065.

Raptis, I., Glezos, N., & Hatzakis, M. (1993) Analytical evaluation of the energy deposition function in electron-beam lithography in the case of a composite substrate. *J.Vac. Sci. & Technol. B.,* Vol. 11, pp. 2754-2757.

Raptis, I., Glezos, N., Valamontes, E., Zervas, E. & Argitis, P. (2001) Electron beam lithography simulation for high resolution and high-density patterns. *Vacuum*, Vol. 62, pp. 263-271.

Scheinhardt-Engels, S. M. , Leermakers, F. A. M. & Fleer, G. J. (2003) Lattice mean-field method for stationary polymer diffusion. *Phys. Rev. E*. Vol. 68, Art. 011802, pp. 1-15.

Schock, K.-D., Prins, F.E., Strähle, S., & Kern, D.P., (1997) Resist processes for low-energy electron-beam lithography. *J.Vac. Sci. & Technol. B.,* Vol. 15, pp. 2323-2326.

Stepanova, M., Dew, S.K., Kovalenko, A. & Aktary, M. (2007). Collaborative Project: 3D simulator of exposure and development in EBL. *Interim report.* NINT & University of Alberta, May 2007, Edmonton, Alberta, Canada.

Tan, Z., Xia, Y., Liu, X, & Zhao, M. (2005) Monte-Carlo simulation of low-energy electron scattering in PMMA using stopping powers from dielectric formalism. *Microelectronic Engineering*, Vol. 77, 285-291.

Word, M.J., Adesida, I. (2003) Nanometer-period gratings in hydrogen silsesquioxane fabricated by electron beam lithography. *J.Vac.Sci.& Technol. B*. Vol. 21, pp.L12-L15.

Wu, B. & Neureuther, A.R. (2001) Energy deposition and transfer in electron-beam lithography. *J.Vac. Sci. & Technol. B,* Vol. 19, pp. 2508–511.

Yan, M., Choi, S. Subramanian, K.R.V., & Adesida, I. (2008) The effects of molecular weight on the exposure characteristics of polymethylmethacrylate developed at low temperatures. *J.Vac. Sci. & Technol. B*. Vol. 26, pp. 2306-2310.

Yasin, S. Hasko, D.G., & Ahmed, H. (2002) Comparison of MIBK/IPA and water/IPA as PMMA developers for electron beam nanolithography. *Microelectronic Engineering*. Vol. 61-62, pp. 745-753.

Yasin, S. Hasko, D.G., Khalid M.N., Weaver, D.J., & Ahmed, H. (2004) Influence of polymer phase separation on roughness of resist features. *J.Vac. Sci. & Technol. B.* Vol. 22 pp. 574-578.

Zhou J. & Yang X. (2006) Monte Carlo simulation of process parameters in electron beam lithography for thick resist patterning. *J.Vac. Sci. & Technol.B.,* Vol.24, pp.1202-1209.

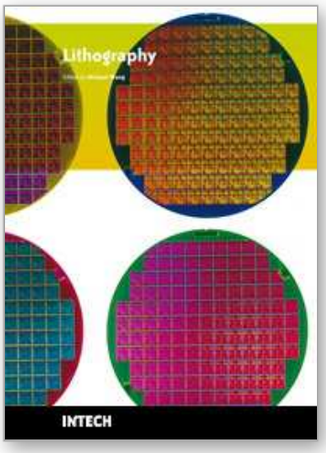

Lithography

Edited by Michael Wang

ISBN 978-953-307-064-3
Hard cover, 656 pages
Publisher InTech
Published online 01, February, 2010
Published in print edition February, 2010

Lithography, the fundamental fabrication process of semiconductor devices, plays a critical role in micro- and nano-fabrications and the revolution in high density integrated circuits. This book is the result of inspirations and contributions from many researchers worldwide. Although the inclusion of the book chapters may not be a complete representation of all lithographic arts, it does represent a good collection of contributions in this field. We hope readers will enjoy reading the book as much as we have enjoyed bringing it together. We would like to thank all contributors and authors of this book.

InTech Europe
University Campus STeP Ri
Slavka Krautzeka 83/A
51000 Rijeka, Croatia
Phone: +385 (51) 770 447
Fax: +385 (51) 686 166
www.intechopen.com

InTech China
Unit 405, Office Block, Hotel Equatorial Shanghai
No.65, Yan An Road (West), Shanghai, 200040, China
中国上海市延安西路65号上海国际贵都大饭店办公楼405单元
Phone: +86-21-62489820
Fax: +86-21-62489821

IntechOpen